Title

Meso-Structure Controlled Synthesis of Sodium Iron-Manganese Oxides Cathode for Low-Cost Na-Ion Batteries

Permalink

https://escholarship.org/uc/item/08z4b6wz

Journal

Journal of The Electrochemical Society, 166(12)

ISSN

0013-4651

Authors

Hirsh, Hayley
Olguin, Marco
Chung, Hyeseung
et al.

Publication Date

2019

DOI

10.1149/2.0701912jes

Peer reviewed

Meso-Structure Controlled Synthesis of Sodium Iron-Manganese Oxides Cathode for Low-Cost Na-Ion Batteries

Hayley Hirsh, ● Marco Olguin, Hyeseung Chung, Yixuan Li, Shuang Bai, Di Feng, Dongdong Wang, Minghao Zhang,*,z and Ying Shirley Meng**,z

Department of NanoEngineering, University of California San Diego, La Jolla, California 92093-0448, USA

A modified co-precipitation method is introduced to synthesize P2-type $Na_{0.67}Fe_{1/4}Mn_{3/4}O_2$ cathode for low-cost Na-ion batteries. The meso-structure of the obtained material is well controlled through regulated cooling after a high temperature calcination process. The material via slow-cooling consists of sphere-like secondary particles with a uniform dispersion while the quenched material exhibits a hexagonal plate-like primary particle without meso-structure. Meso-structure is found to have a distinct effect upon the electrochemical performance of P2-type layered cathode. The slow-cooled sample exhibits a larger capacity and improved cyclability compared with the quenched sample, which is attributed to the larger surface area, reduced surface contamination, and surprisingly higher transition metal redox activity. This work demonstrates that cooling rate plays the key role in controlling the formation of spherical meso-structure for sodium iron-manganese oxides with enhanced electrochemical performance.
© 2019 The Electrochemical Society. [DOI: 10.1149/2.0701912jes]

Solar and wind as sustainable and renewable energy sources have attracted considerable attention in recent years. To expand the generation of electrical energy from these highly intermittent energy sources in nature, large-scale inexpensive energy storage has gained great interests from the scientific and community at large.[1] Batteries are considered as the most promising technology for next-generation grid storage due to their high energy density, low operation cost, and long cycle life. Among all the state-of-the-art batteries, Na-ion batteries (NIBs) have a tantalizing possibility for commercial grid storage, by reason of the abundant availability of its sources and the suitable redox potential ($E_{(Na+/Na)} = -2.71$ V vs. SHE).[2]

Various types of NIB cathode materials have been investigated in the past few decades including layered oxides, poly-anionic frameworks, hexacyanoferrates, and organics.[3–8] Among these cathode materials, layered oxide materials Na_xTMO_2 (TM = Mn, Co, Fe, Ni, Ti, Cu, Cr or mixtures of the elements) are one of the most favorable candidates due to their large capacities and tunable properties.[3] In the wide range of choices for TMs in sodium layered oxides, Li, Ni, and Co are rather expensive elements while Fe and Mn are low-cost and abundant. For NIBs to be viable, the components of the cathode material should include only inexpensive elements in the ideal case. Sodium iron manganese oxides $Na_xFe_{1-y}Mn_yO_2$ have already shown promising initial discharge capacities.[9] For example, P2-type layered $Na_{2/3}Mn_{1/2}Fe_{1/2}O_2$ and $Na_{2/3}Fe_{1/3}Mn_{2/3}O_2$ are able to deliver first discharge capacities of 200 mAh/g in the voltage range 1.5–4.3 V (vs. Na^+/Na^0).[9] However, the practical and commercial applications of $Na_xFe_{1-y}Mn_yO_2$ are hindered because of their poor capacity retention over cycling.[2]

Previous studies have identified several factors contributing to this poor capacity retention, including irreversible phase changes, particle defects and particle pulverization.[9] Correspondingly, modification strategies including TM substitution and surface coating have been put forward to improve the cycling performance.[10–12] These two approaches often involve either complex synthesis processes such as atomic layer deposition, or introduce costly elements such as Co and Ni.[10–12] Meso-structure control synthesis, on the other hand, can reduce the occurrence of both irreversible phase change and particle pulverization without significant process adaptation.[13,14] As demonstrated in lithium ion batteries, micron sized spherical meso-structures consisting of nanosized primary particles could enable faster Li ion diffusion and at the same time provide enhanced particle strain management, thus mitigating mechanical degradation and improving capacity retention.[13–24]

The synthesis method strongly influences the meso-structure of the layered TM oxides. In reviewing the literature (Table I),[25–36] solid-state synthesis is the most frequently adopted method for $Na_xFe_{1-y}Mn_yO_2$. However, the meso-structure is difficult to control in solid-state synthesis since it entails mixing materials by either ball milling or hand grinding precursors followed by high temperature calcination, producing irregular or plate-like primary particles. Similarly, no meso-structure controlled samples were found in previous work via auto-combustion and sol-gel synthesis methods.[32,33,35] The co-precipitation method, which is commonly used to synthesize spherical secondary particles for lithium TM oxides, was not previously reported to obtain meso-structure controlled $Na_xFe_{1-y}Mn_yO_2$ (Table II).[15,34,37,38] In the cases where co-precipitation method was applied for sodium iron manganese oxides, the resulting materials were plate-like.

In this study, pure phase P2-type $Na_{0.67}Fe_{1/4}Mn_{3/4}O_2$ with a spherical meso-structure was synthesized through modified co-precipitation method for the first time. To enable the formation of the desired meso-structure $Na_{0.67}Fe_{1/4}Mn_{3/4}O_2$, spherical precursors $Fe_{1/4}Mn_{3/4}CO_3$ were synthesized under optimized conditions such as suitable pH value and N_2 atmosphere. It is found that cooling rate played an important role in controlling the meso-structures of the final product. A pure phase P2-type $Na_{0.67}Fe_{1/4}Mn_{3/4}O_2$ was made into hexagonal plates with no secondary structure by quenching or into a sphere-like meso-structure by slow-cooling. The formation of meso-structure enables fast Na diffusion as well as a reduced surface concentration of sodium carbonate which lowers resistance during cycling. Both features can effectively minimize capacity loss of sodium layered oxides during long-term cycling. This comparison of different morphologically controlled samples will determine a future direction of designing improved NIB cathode materials.

Methods

Materials preparation.—The synthesis set-up for pure phase P2-$Na_{0.67}Fe_{1/4}Mn_{3/4}O_2$ (NFMO) is shown in Figure 1. Stoichiometric amounts of the precursors, $Fe(SO_4) \cdot 7H_2O$ and $Mn(SO_4) \cdot H_2O$ (Fe:Mn = 1:3 in molar ratio) were dissolved in deionized water for a total concentration of 1 M. TM sulfate solution and an aqueous solution of 0.2 M Na_2CO_3 were separately pumped into a reaction vessel to maintain the pH value at 8.8. The reaction was stirred continuously with N_2 bubbled through the reaction vessel. The obtained mixture was aged at 80°C for 12 hours. The resulting $Fe_{1/4}Mn_{3/4}CO_3$ was washed with deionized water to remove residual Na^+ and dried at 80°C overnight. $Fe_{1/4}Mn_{3/4}CO_3$ powder was then mixed with a 5% excess stoichiometric ratio of Na_2CO_3 and the mixture was calcinated at 900°C for 15 hours in air. For quenched samples, the crucible was taken out of the furnace directly after the 15 hours calcination and cooled in air on a metal plate. For the slow-cooled

*Electrochemical Society Student Member.
**Electrochemical Society Fellow.
zE-mail: miz016@eng.ucsd.edu; smeng@ucsd.edu

Table I. Synthesis parameters for sodium iron manganese oxide cathode materials reported from literature.

Composition	Phase	Synthesis type	Mn precursor	Fe precursor	Na precursor	Calc. Temp (C)	Calc. time (h)	quenched?	atm?	morphology	citation #
$Na_{2/3}Fe_{1/2}Mn_{1/2}O_2$	P2	Solid State	Mn_2O_3	Fe_2O_3	Na_2O_2	900	12	Y	air	irregular	25
$Na_{2/3}Fe_{1/3}Mn_{2/3}O_2$	P2	Solid State	Mn_2O_3	Fe_2O_3	Na_2O_2	900	12	Y	air	irregular	26
$Na_{2/3}Fe_{1/2}Mn_{1/2}O_2$	P2	Solid State	$C_4H_6MnO_4x4H_2O$	$C_6H_5O_7FexH_2O$	Na_2CO_3	800	8	Y	air	plates	27
$Na_{0.67}Mn_{0.5}Fe_{0.5}O_2$	P2	Solid State	Mn_2O_3	Fe_2O_3	Na_2CO_3	750, 900	4, 6	N	air	irregular	28
$Na_{0.67}Mn_{0.5}Fe_{0.5}O_2$	P2	Solid State	Mn_2O_3	Fe_2O_3	Na_2CO_3	900	12	N	air	irregular	29
$Na_{0.67}Mn_{0.5}Fe_{0.5}O_2$	P2	Solid State	Mn_2O_3	Fe_2O_3	Na_2CO_3	450, 900	6, 15	N	air	irregular	30
$Na_{2/3}Fe_{1/2}Mn_{1/2}O_2$	O3	Solid State	Mn_2O_3	Fe_2O_3	Na_2O_2	700	36	Y	air	irregular	25
$NaFe_{0.5}Mn_{0.5}O_2$	O3	Solid State	Mn_2O_3	Fe_2O_3	Na_2CO_3	900	24	N	air	unknown	31
$NaFe_{0.5}Mn_{0.5}O_2$	O3	Solid State	Mn_2O_3	Fe_2O_3	Na_2CO_3	700	36	N	air	irregular	29
$Na_{2/3}Fe_{1/2}Mn_{1/2}O_2$	P2	Autocombustion	$Mn(NO_3)_2x4H_2O$	$Fe(NO_3)_3x9H_2O$	$NaNO_3$	1000	6	N	air	plates	32
$Na_{0.81}Fe_{0.5}Mn_{0.5}O_2$	O3	Autocombustion	$Mn(NO_3)_2x4H_2O$	$Fe(NO_3)_3x9H_2O$	$NaNO_3$	700, 1000	20, 5	Y	O2	irregular	33
$Na_{0.77}Fe_{2/3}Mn_{1/3}O_2$	O3	Autocombustion	$Mn(NO_3)_2x4H_2O$	$Fe(NO_3)_3x9H_2O$	$NaNO_3$	700, 1000	20, 5	Y	O2	irregular	33
$Na_{0.77}Fe_{2/3}Mn_{1/3}O_2$	P2	Autocombustion	$Mn(NO_3)_2x4H_2O$	$Fe(NO_3)_3x9H_2O$	$NaNO_3$	700, 1000	20, 5	Y	O2	plates	33
$Na_{0.67}Mn_{0.5}Fe_{0.5}O_2$	P2	Autocombustion	$Mn(NO_3)_2x4H_2O$	$Fe(NO_3)_3x9H_2O$	$NaNO_3$	700, 1000	20, 5	Y	O2	plates	33
$Na_{2/3}Fe_{1/2}Mn_{1/2}O_2$	O3	Co-precipitation	$Mn(NO_3)_2$	$Fe(NO3)3$	$NaOH$	700	1	N	air	plates	34
$Na_{2/3}Fe_{1/2}Mn_{1/2}O_2$	P2	Co-precipitation	$Mn(NO_3)_2$	$Fe(NO3)3$	$NaNO_3$	900	6	N	air	plates	34
$Na_{2/3}Fe_{1/2}Mn_{1/2}O_2$	P2	Sol-Gel	$Mn(CH_3COO)_2$	$Fe(NO_3)_3x9H_2O$	$NaNO_3$	900	12	N	O2	plates	35
$Na_{0.67}Mn_{0.6}Fe_{0.4}O_2$	P2	Acetate Decomposition	$Mn(Ac)_2$	$Fe(Ac)_2$	$NaAc$	450, 900	7, 12	N	air	plates	36

samples, after the 15 hours calcination time the furnace was set to cool down to room temperature over 12 hours.

Materials characterization.—The crystal structures were characterized by X-ray diffraction (XRD) using a Bruker D8 advance diffractometer with copper Kα source or Mo Kα source. Rietveld refinement was applied to the obtained diffraction pattern using FullProf software. The morphology and meso-structure of the particles were identified by using a Zeiss Sigma 500 scanning electron microscope (SEM) with an accelerating voltage of 1 kV for the carbonate precursors and 3 kV for the TM oxides. Surface area of the particles was determined using nitrogen physisorption by the Brunauer–Emmett–Teller (BET) method. ICP-OES was performed using a Perkin Elmer 3000 DV optical emission plasma spectrometer. X-ray photoelectron spectroscopy (XPS) was performed using an AXIS Supra by Kratos Analytica. The XPS was operated using an Al anode source at 15 kV, scanning with step size of 0.1 eV and 200 ms dwell time. Fits of the XPS spectra were performed with CasaXPS software to estimate the oxidation states of the TMs. Sodium carbonate titration was performed by washing 1 g of cathode material with 10 mL of DI water. The resulting solution was separated from the powder by filtration. The surface contamination content was determined using a titration method with 0.05 M HCl. The titration was monitored with a pH probe to an end pH of 8.0. Electron microscopy work was carried out on a JEOL-2800 TEM/SEM microscope. TEM images were acquired at 200 kV.

Electrochemical characterization.—Composite cathode electrodes were prepared by mixing a slurry of active material, acetylene carbon black, and polyvinylidene fluoride (PVDF) in a weight ratio of 8:1:1, with n-methyl-2- pyrrolidone. The slurry was cast onto aluminum foil and dried under vacuum at 80°C overnight. Na metal was used as the counter electrode with 1 M $NaPF_6$ in PC as the elec-

trolyte and glass fiber GF/D (Whatman) as the separator. The electrodes were assembled in 2032 coin cells in an argon filled glove box ($H_2O < 0.1$ ppm) and tested on an Arbin battery cycler. Coin cells were allowed to rest 8 h before electrochemical tests were performed. The voltage range was maintained between 1.5–4.3 V and C-rates were calculated by assuming a theoretical specific capacity of 120 mAh/g. Additionally, electrochemical spectroscopy (EIS) measurements were carried out with 10 mV perturbation and AC frequencies from 0.01 to 1×10^6 Hz on galvanostatic cycled electrodes charged to 4.3 V and discharged to 1.5 V during the first cycle. A Solartron 1287 Potentiostat was used to measure impedance at different states of charge. An equivalent circuit model was used to fit the data and analyze the reactions using Zview software (v. 3.4a, Scribner Associates, Inc.).

Computational study.—Electronic structure calculations were performed within the framework of periodic planewave density functional theory (DFT) using the Vienna ab initio Simulation Package (VASP.5.4.4) for three different Na/Fe/Mn/O based model cathode systems. Both GGA+U and hybrid density functionals were employed for Density of States (DOS) calculations. The GGA+U calculations employed the spin-polarized Perdew-Burke-Ernzerhof (PBE) exchange-correlation functional with the projector-augmented wave (PAW) scheme to treat core electrons. For the +U augmented treatment of Fe and Mn 3d orbitals, we chose U_{eff} values given on the Materials Project of 5.3 eV for Fe and 3.9 eV for Mn. The corresponding U_{eff} values for Fe and Mn capture the Fe^{2+}/Fe^{3+} and Mn^{2+}/Mn^{4+} redox couple, respectively, in transition metal oxides. The PAW pseudopotentials employed for the transition metal atoms Fe and Mn (denoted as Fe_pv and Mn_pv, respectively) treat p semi-core states as valence states. The Na_sv pseudopotential used for Na treats the 2s shell as valence states. The standard pseudopotential was used for oxygen. Anti-ferromagnetic coupling between magnetic Fe and Mn cations was assumed. A planewave energy cutoff of 600 eV was employed in

Table II. Co-precipitation synthesis parameters of iron containing sodium TM oxides cathode materials reported from literature.

Composition	Phase	Precursor type	Mn precursor	Fe precursor	Na precursor	Other precursor	Morphology	pH	Citation #
$Na_{2/3}Fe_{1/2}Mn_{1/2}O_2$	P2	-	$Mn(NO_3)_2$	$Fe(NO_3)_3$	$NaNO_3$	-	plates	10	34
$Na_{2/3}Fe_{1/2}Mn_{1/2}O_2$	O3	-	$Mn(NO_3)_2$	$Fe(NO_3)_3$	$NaOH$	-	plates	10	34
$NaNi_{0.2}Fe_{0.55}Mn_{0.25}O_2$	O3	oxalate	$MnSO_4·H_2O$	$FeSO_4·7H_2O$	Na_2CO_3	$(NH_4)C_2O_4, NiSO_4·6H_2O, NH_4OH$	irregular	7	37
$NaNi_{1/3}Fe_{1/3}Mn_{1/3}O_2$	O3	oxalate	$MnSO_4·H_2O$	$FeSO_4·7H_2O$	Na_2CO_3	$NiSO_4·6H_2O, Na_2C_2O_4$	unknown	-	38
$NaNi_{1/3}Fe_{1/3}Mn_{1/3}O_2$	O3	hydroxide	$MnSO_4·H_2O$	$FeSO_4·7H_2O$	Na_2CO_3	$NaOH, NH_3, NiSO_4·6H_2O$	plates	10.5	15

Figure 1. Schematic of the modified co-precipitation synthesis process for meso-structure controlled sodium iron manganese oxide.

all calculations. Cell relaxation calculations (ISIF = 3) at the PBE+U level plus Grimme's D3 dispersion correction on the Na/Fe/Mn/O bulk structures were performed using a 10^{-4} eV energy convergence criterion with a $5 \times 5 \times 3$ k-point grid. In order to obtain a high-accuracy electronic DOS, the Heyd−Scuseria−Ernzerhof (HSE06) hybrid functional with 25% exact exchange was used for single-point energy calculations on PBE+U-D3 optimized structures. The single-point energy DOS calculations were performed using a 10^{-5} eV energy convergence criterion with a $12 \times 12 \times 6$ k-point grid for PBE+U calculations and a $4 \times 4 \times 2$ k-point grid for HSE06 calculations. To obtain a high-resolution DOS within an energy window bracketing the Fermi level, we set the energy range for evaluation of the DOS to -10 eV to $+10$ eV with 2001 grid points (EMIN = -10; EMAX = 10; NEDOS = 2001).

Results and Discussion

The co-precipitation method for pure phase meso-structure controlled NFMO begins with obtaining a spherical TM carbonate pre-cursor without hydroxide or other impurities. Two factors, pH value and nitrogen bubbling, are critical to synthesize pure phase carbonate precursor with desired TM ratio (see SI for details). In short, residual TM ions will be found if the solution is too acidic, and hydroxide impurities will form if the co-precipitation occurs without nitrogen bubbling. A pure carbonate precursor was finally obtained with pH controlled at 8.8 and continuous N_2 bubbling through the reaction vessel. After high temperature calcination, NFMO samples were ei-ther quenched or slow-cooled to obtain the final product. Figure 2 shows a comparison between the quenched and slow-cooled NFMO including XRD data, SEM images, and a table of parameters including XRD refinement results, BET surface area, and ICP-OES measure-ments. In both samples, all the diffraction peaks can be well indexed to space group $P6_3/mmc$. The Rietveld refinement results confirm that both samples are pure phase P2 layered material with similar lattice parameters. According to a classification by Delmas et al., P2-type layered structure has ABBA oxygen stacking sequence where Na ions are located in trigonal prismatic (P) sites.[39] The ICP-OES results show that both samples have the same designed stoichiometric ratio. These

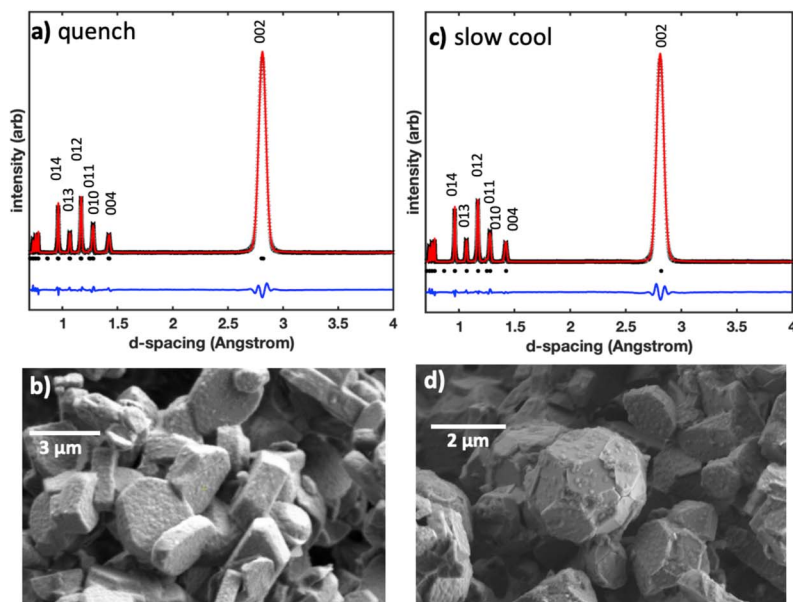| e)	quench	slow cool
a=b (Å)	2.916	2.916
c (Å)	11.255	11.186
Rwp (%)	5.51	4.54
Rb (%)	7.49	5.95
O position	(1/3, 2/3, 0.0891)	(1/3, 2/3, 0.0891)
surface area (m²/g)	1.06 +/- 0.021	1.55 +/- 0.031
Fe:Mn	0.33(2)	0.33(2)

Figure 2. XRD and SEM of quenched NFMO (a, b) and slow-cooled NFMO (c, d) show that the two materials have the same crystal structure but different morphology and meso-structures. Selected parameters from XRD refinement, BET, and ICP measurements for the two materials are shown in (e).
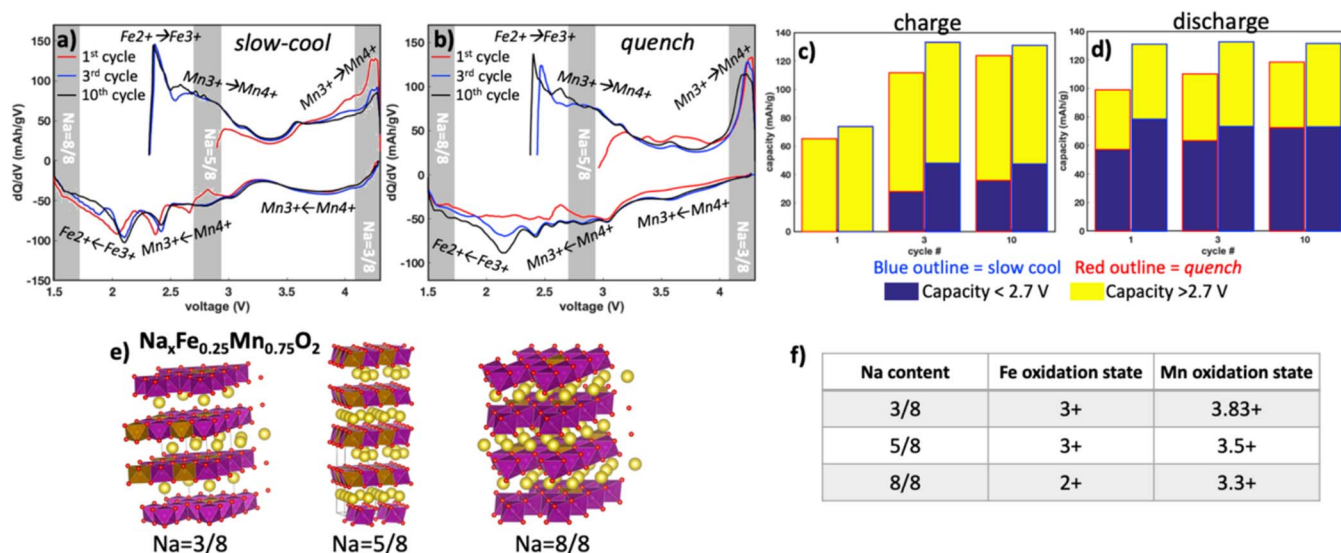
Figure 3. dQ/dV curves of the 1st, 2th, and 10th cycles of slow-cooled (a) and quenched (b) NFMO at a rate of C/50. Bar graphs representing the charge (c) and discharge (d) capacities between 1.5–2.7 V and 2.7–4.3 V at different cycles for slow-cooled and quenched NFMO. Model structures of P2-$Na_xFe_{0.25}Mn_{0.75}O_2$, where x = 3/8, 5/8 and 8/8 (e) were used to calculate average Fe and Mn oxidation states of their respective structures (f).

results quantitatively reveal that NFMO samples synthesized by different cooling rate are similar in terms of bulk structure and chemical composition.

The main differences between the two samples are the different meso-structures and specific surface areas. As shown in Figures 2b and 2d, the quenched NFMO contains hexagonal plate-like particles that are 1–5 μm in diameter and less than a micron thick. While the slow-cooled NFMO has a well-controlled meso-structure containing ~500 nm hexagonal plate-like primary particles and 2–3 μm secondary sphere-like particles (SI Figure 5). It is hypothesized that the quenched material retained too much stress which leads to breakdown of the spherical particles, although we cannot exclude other possibilities. Further experiments are in progress to explore the relationship between cooling rate and meso-structure formation in NFMO. The specific surface area of both samples was also determined by BET adsorption measurements. Plate-like NFMO sample has a specific surface area of 1.06 +/− 0.021 m^2/g, while meso-structure controlled NFMO has a higher number of 1.55 +/− 0.031 m^2/g. The higher surface area of slow cooled NFMO can be attributed to smaller primary particle size and porosity between primary particles.

To probe the mechanisms of sodium intercalation/deintercalaction from NFMO, dQ/dV studies were coupled with DFT calculations of the TM oxidation states in NFMO at different states of charge (see Figure 3). In pristine NFMO (Na = 5/8), DFT predicts the average oxidation states for Fe and Mn are 3+ and 3.5+ respectively, determined by the magnetization output. When 2/8 Na are removed from the prisine structure, representing the first charge state, the calculated capacity is 65 mAh/g. This value for the first charge matches well with the experimental value for both quenched and slow-cooled NFMO (Figure 3c). The Fe oxidation state does not change during this first charge while the average Mn oxidation state changes from 3.5+ to 3.83+, which indicates that solely Mn is redox active. When discharging NFMO from fully charged state (Na = 3/8) to the fully discharged state (Na = 8/8), the total calculated discharge capacity is 163 mAh/g. This calculated discharge capacity is larger than the experimental capacity for quenched and slow-cooled NFMO shown in Figure 3d. During the discharge to Na = 8/8, Fe is calculated to reduce from 3+ to 2+ and Mn is calculated to reduce from 3.5+ to 3.3+. In the model when Na = 8/8 (Figure 3e), 4/18 Mn 3+ atoms are calculated to be in the high spin state, signifying they are Jahn-Teller active. If these four Mn atoms do not reduce to the 3+ state, the discharge capacity is reduced by 32.5 mAh/g, resulting in the calculated discharge capacity to be 131 mAh/g. This discharge capacity matches the experimental 10th

discharge capacity of slow-cooled NFMO, suggesting that this model is a valid representation of the NFMO system. Additionally, the good cycling retention for NFMO (Figures 4c, 4d) can be attributed to the fact that all the Mn 3+ in this system are not Jahn-Teller active.

From DFT calculations of NFMO at different states of charge, the TM redox can be attributed to different regions of the dQ/dV curve. In the high voltage region (Na = 5/8 to Na = 3/8) only the Mn 3+/4+ redox couple is active while in the low voltage region (Na = 5/8 to Na = 8/8) both the Fe 2+/3+ and Mn 3+/4+ redox couples are active (see pDOS in SI Figure 6). The low voltage peaks in the slow-cooled NFMO dQ/dV (Figures 3a, 3b) are initially larger than the peaks in the quenched NFMO dQ/dV. This indicates that the Fe redox couple is initially more active for slow-cooled NFMO than for quenched NFMO and is corroborated by the larger capacity in the low voltage region (1.5–2.7 V) for slow-cooled NFMO (Figures 3c, 3d). Additionally, for the quenched NFMO, the low voltage peaks in the dQ/dV curve increase in size and the capacity from the low voltage region increases from the 1st cycle (discharge capacity = 57.4 mAh/g) to the 10th cycle (discharge capacity = 72.58 mAh/g). At the 10th cycle, the discharge capacity in the 1.5–2.7 V region are almost equivalent for quenched NFMO (72.58 mAh/g) and slow-cooled NFMO (73.2 mAh/g), signifying that the Fe redox couple is kinetically limited for quenched NFMO. The same trend is observed during charging in the low voltage region for quenched NFMO, although the capacity is still less than that of the slow-cooled NFMO. These observations indicate Fe redox couple has sluggish kinetcs and has limited activity for quenched NFMO.

To further compare the electrochemical performance of quenched and slow-cooled NFMO, half cells with sodium metal as the anode were assembled and cycled in galvanostatic mode. Figure 4a shows the first cycle voltage profile of both NFMO samples. Both samples have larger discharge capacity than charge capacity, which implies more Na ions intercalate back to the cathode materials compared to the original state. The quenched sample delivers a first discharge capacity of 100 mAhg^{-1} in the voltage range of 1.5–4.3 V at a rate of C/50 compared to slow-cooled NFMO which delivers a first discharge capacity of 131 mAh/g. After 10 cycles, slow-cooled NFMO still delivers higher discharge capacity of 132 mAh/g compared to 119 mAh/g of quenched NFMO, as shown in Figure 4b. This large difference in discharge capacity can be explained by bulk and surface difference in the quenched and slow-cooled NFMO materials: (1) Fe has redox couple has sluggish kinetics for quenched NFMO, (2) there are disparities in the surface area and surface contamination of sodium carbonate. Based on BET data in Figure 2e, it is determined that
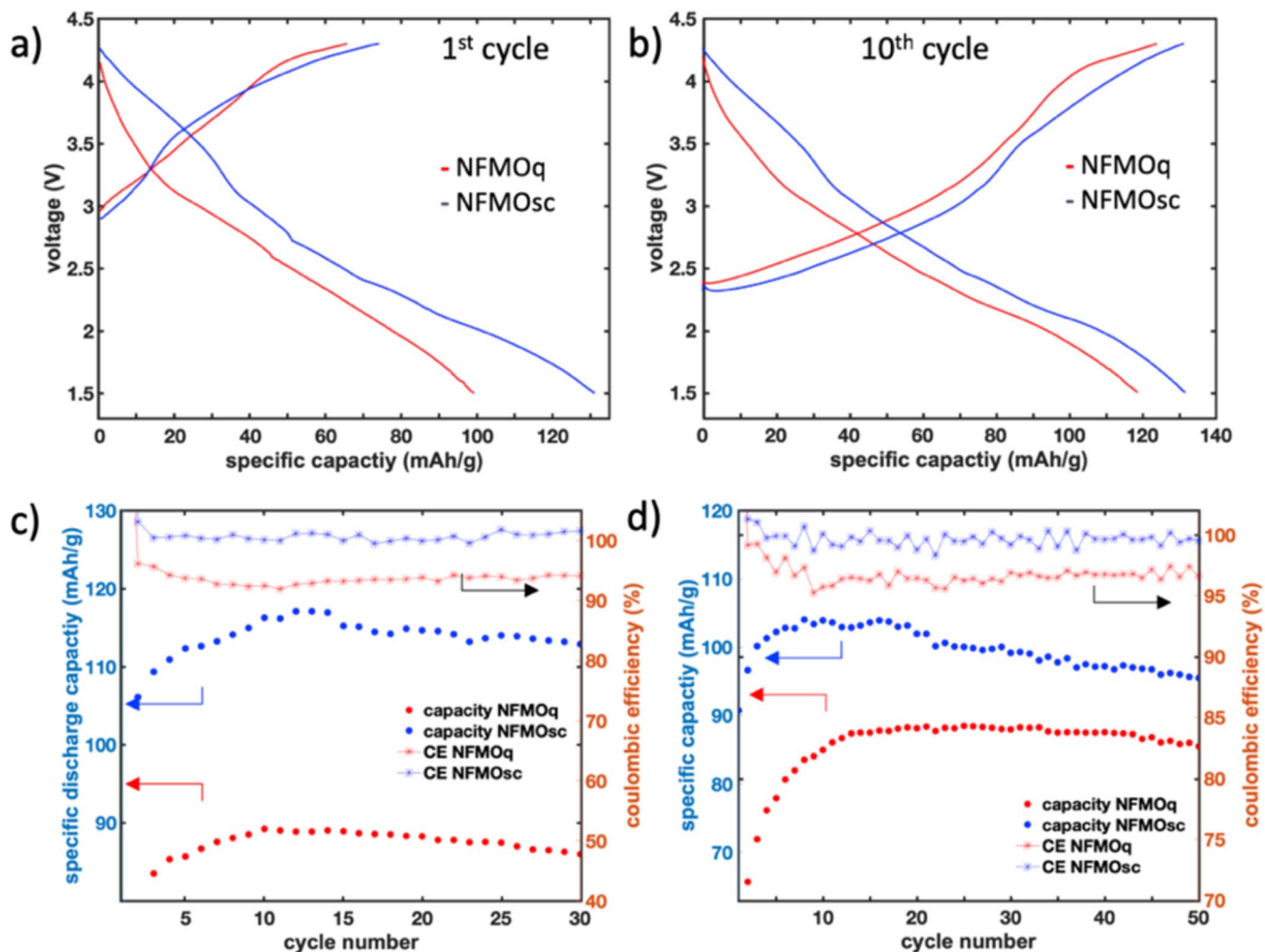
Figure 4. Voltage profiles for quenched and slow-cooled NFMO at a rate of C/50 at (a) cycle 1 and (b) cycle 10. Specific discharge capacity versus cycle number at a rate of (c) C/20 and (d) C/10 and coulombic efficiency as a function of cycle number.

slow-cooled NMFO material has a 46% larger surface area than quenched NFMO material. This increase in surface area allows for more pathways for Na ion diffusion to the bulk of material, and thus improves discharge capacity. The small capacity fade observed for both materials could be caused by the formation of stacking faults during cycling, as reported by Yabuuchi.[25] The capacity fade of NFMO is one of the lowest of $Na_xFe_yMn_{1-y}O_2$ cathode materials reported in literature.[25–36] The low capacity fade of the materials reported here can be attributed to the low Fe content and potentially lower sodium carbonate surface contamination. Fe in the TM layer has been reported to increase the sodium carbonate contamination on Na TM layered oxides,[28] however quantification of the sodium carbonate contamination is not commonly reported in cathode literature.

Additionally, in cycling tests, slow-cooled NFMO also shows higher coulombic efficiency at rates of C/20 and C/10 (Figures 4c, 4d and SI Figure 7). The difference in coulombic efficiency manifests that slow-cooled NFMO has better capacity retention over cycling. The low coulombic efficiency of quenched NFMO could be caused by continual decomposition of electrolyte near the surface of quenched NFMO during charging, triggered by excess sodium carbonate surface contamination.[28] Slow-cooled NFMO has significantly higher coulombic efficiency that fluctuates around 100% (fluctuations likely caused by temperature changes in the laboratory) after the first cycle. The significant difference in the coulombic efficiency between quenched and slow-cooled NFMO can be attributed to the differences in their surface chemistry.

XPS was applied to investigate differences in the surface chemistry between the slow-cooled and quenched NFMO samples (see Figure 5). Figure 5a shows each material's Mn 3s regions. Previous work has demonstrated that splitting between the main Mn 3s peak and its satellite is highly sensitive to the Mn valence state.[38] The larger the splitting, the lower its oxidation state. From the Mn 3s spectra, the oxidation state of Mn is 4+ for both samples as indicated by the 4.8 eV peak separation.[40] Figure 5b show the Fe 2p region for each material. The binding energy of Fe 2p peaks and their satellites shift to higher binding energy for increased oxidation state.[41,42] A combination of peaks for Fe^{2+} and Fe^{3+} were fit to the experimental data to determine the percentage of the oxidation states in the sample. Iron is a mix of two oxidation states, 2+ and 3+, with slow-cooled sample containing 36% Fe^{2+} and quenched sample containing 30% Fe^{2+}.[43] The discrepancies in these values from the DFT results can be attributed to surface modifications or reactions. Based on these results, TM oxidation states on the surface are essentially identical for slow-cooled and quenched NFMO sample. Other surface factors, such as sodium carbonate surface contamination can contribute to the differences in performance between slow-cooled and quenched NFMO.

Sodium carbonate is a common surface contaminant on sodium TM oxide cathodes and can form on the surface of the cathode particles through sodium's reaction with air during synthesis.[43,44] It is hypothesized that sodium carbonate forms preferentially on the edges of the TM layers ((1 0 0) plane) instead of the hexagonal surfaces ((0 0 1) plane). The sodium diffusion channels are perpendicular to
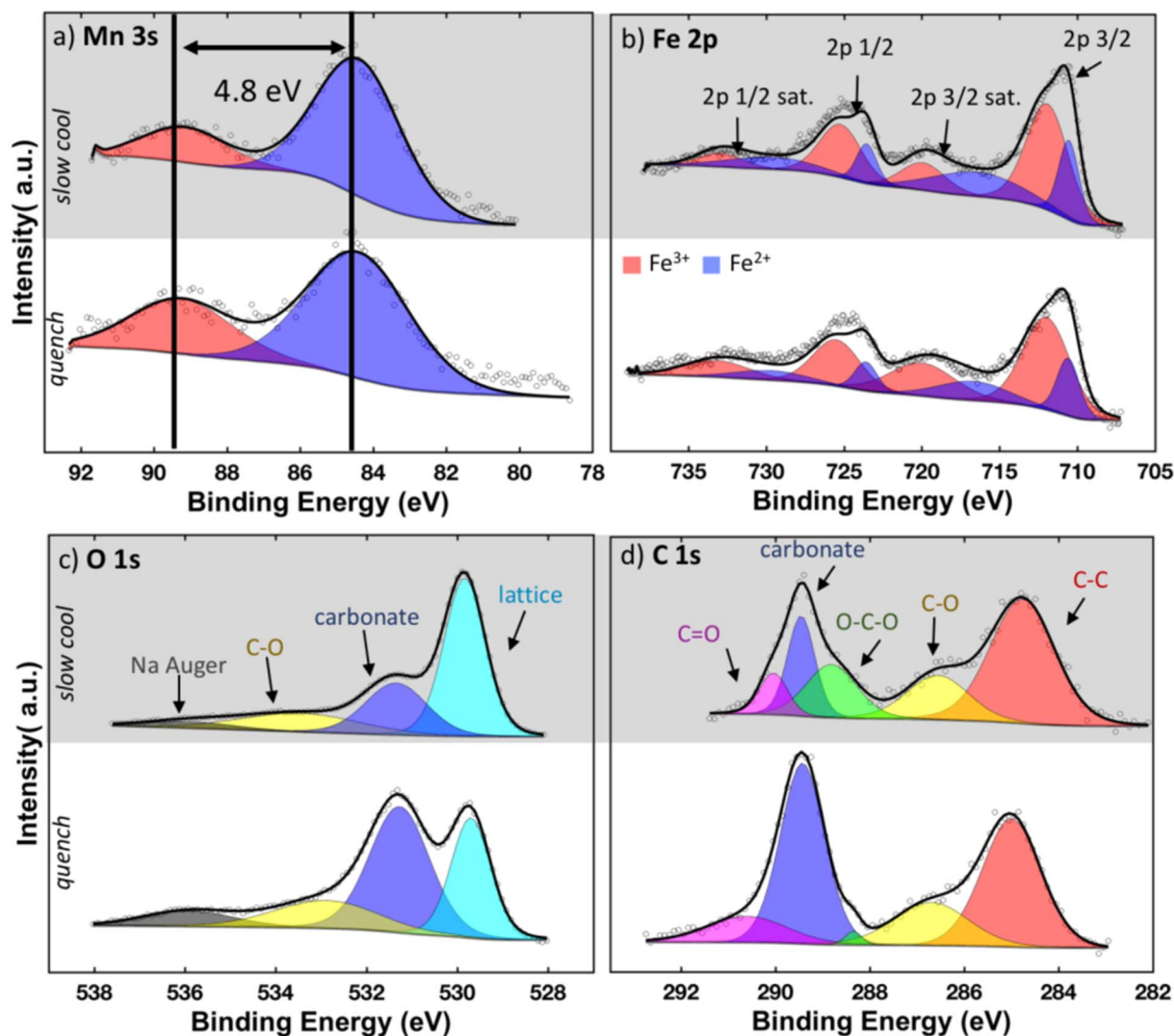
Figure 5. XPS spectra of (a) Mn 3s, (b) Fe 2p, (c) O 1s, and (d) C 1s regions for slow-cooled (gray background) and quenched (white background) NFMO.

the (1 0 0) plane, which could promote the formation of sodium carbonate during synthesis. Additionally, the (1 0 0) planes of slow-cooled NFMO primary particles are less exposed than the quenched NFMO particles, given slow-cooled NFMO sphere-like meso-structure (Figure 2d). The minimization of the (1 0 0) plane exposure of slow-cooled NFMO may explain the lower concentration of sodium carbonate on the surface. The mechanism of sodium carbonate formation on the surface of sodium layered oxide cathodes is currently under investigation by DFT surface calculations. Sodium carbonate was identified on the surface of both materials based on the O 1s (531.3 eV) and C 1s (289.4 eV) XPS spectra. Interestingly, quenched NFMO has twice the sodium carbonate on its surface as compared to slow-cooled NFMO. This was verified through titration of the surface species and TEM imaging shown in SI Tables 3 and 4 and SI Figure 8. Titration of the surface species for sodium layered cathode materials was used only as a qualitative measurement for two reasons: (1) The initial pH value of the washed cathode solution was higher than the pH of pure concentrated Na_2CO_3 (pH of 11.56 for 10 M). This higher pH value is likely caused by other surface contaminants such as NaOH which can increase the pH beyond 11.56. (2) It has been reported that some sodium layered cathode materials can react with water, causing sodium ions to de-intercalate.[44] This method is considered to adequately compare the surface contamination of materials with the same composition. The XPS, and titration results confirm the quenched NFMO having around twice the surface contamination than that of slow-cooled NFMO. The

increase of surface sodium carbonate on the quenched material could be ascribed to the quenched surface having a higher surface energy. In literature, annealing has been used to decrease the surface energy of cathode material due to increased ordering of the TMs.[45] Further research is being conducted to determine the surface energy and TM ordering in NFMO. Sodium carbonate on the surface of the cathode material could lead to higher resistance during electrochemical reaction, thus lowering the capacity of the cathode. The increase of resistance in quenched NFMO can be evidenced by the average voltage vs. cycle number shown in SI Figure 9. The average voltage during the 10th charge is 3.21 V and 3.13 V for the quenched and slow-cooled NFMO respectively. During the 10th discharge, the average voltage is 2.56 V and 2.70 V for quenched and slow-cooled NFMO respectively. The higher voltage during charging and lower voltage during discharging, known as polarization, is indicative of higher resistance.

The above characterization results demonstrate that both NFMO samples have similar crystallinity and composition, but significantly different morphologies, specific surface area, and surface sodium carbonate concentration. Slow cooling is the key to form spherical meso-structures which could have the following advantages: (1) the robust meso-structures could release particle strain generated during electrochemical cycling; (2) the high specific area could provide more Na ion diffusion pathways; (3) the low surface carbonate concentration could reduce the surface charge transfer resistance. These factors
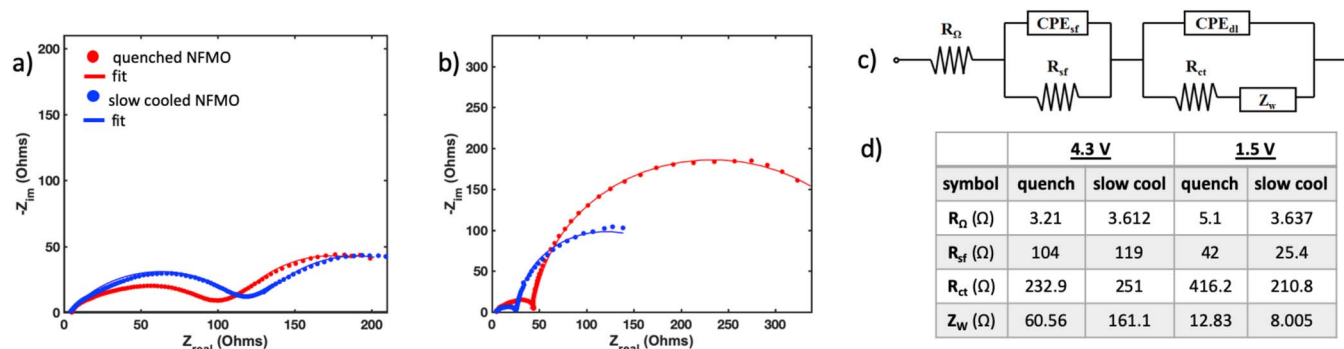
Figure 6. Nyquist plots of quenched and slow cooled NFMO (a) charged to 4.3 V and (b) discharge to 1.5 V. The fit of the data is based on the circuit shown in (c). The table (d) contains the values for the impedance measurements.

together can contribute to an improved electrochemistry performance of NFMO cathode material.[25,46,47]

In order to investigate the electrochemical resistance of both samples, EIS was conducted during the first charging and discharging cycle. The Nyquist plots in Figures 6a and 6b show the real versus imaginary impedance over a range of AC frequencies of both materials as they are charged to 4.3 V and discharged to 1.5 V. The impedance spectra can be quantitatively analyzed using a model circuit shown in Figure 6c. This model accounts for the ohmic resistance of the set-up (R_Ω), the double layer capacitance of the electrode/electrolyte interface (CPE_{sf}), the resistance due to Na ion diffusion through the surface of the cathode (R_{sf}), the double layer capacitance (CPE_{dl}) the charge transfer resistance (R_{ct}) and the impedance of the solid state diffusion of Na ions through the bulk of the active material known as the Warburg impedance (Z_w). From Figures 6a and 6b, the impedance at 4.3 V is comparable for quenched and slow-cooled NFMO. A similar observation was found by G. Zhuang et al. where a cathode heavily contaminated with lithium carbonate had a comparably high resistance to a minimally contaminated cathode.[48] They also observed that after the first charge, the resistance for both materials decreased. For quenched and slow-cooled NFMO there is a decrease in R_{sf} in both materials at 1.5 V. This decrease in resistance could reflect sodium carbonate decomposition at high voltage or dissolution and penetration of the carbonate coating caused by particle volume change. Because of the higher concentration of sodium carbonate on the surface of quenched NFMO, after sodium carbonate decomposition or dissolution, the impedance of quenched NFMO is higher at 1.5 V than the impedance of slow-cooled NFMO. The resulting cathode electrolyte interphase (CEI) caused by excess sodium carbonate on the quenched NFMO surface results in a higher R_{ct} across the CEI. A thick and resistive CEI could impede Na intercalation into the center of the larger primary particles of the quenched NFMO.[49] This mass transport resistance eventually increases cathode overpotential that leads to inferior electrochemical performance during cell cycling.

A key parameter that affects the capacity of NIB cathode materials is the level of surface contamination. Surface contamination can increase resistance and reduce capacity. In literature, besides storing the material in an inert environment, which only stops further contamination, no effective and simple methods are known to reduce surface contamination of NIB cathode materials. Here, we show that through controlling the meso-structure of NFMO, the extent of surface contamination can be minimized. The mechanism of surface contamination for layered NIB cathode materials has not been thoroughly discussed in literature. If surface contamination preferentially forms on certain facets of the cathode crystal structure, then a secondary meso-structure could reduce the exposure of these facets to react with the atmosphere. If the surface contamination forms more readily on un-relaxed surfaces, then the secondary meso-structure obtained by slow cooling could have a more relaxed surface which effectively reduces the surface contamination.

Conclusions

Meso-structure controlled P2-type $Na_{0.67}Fe_{1/4}Mn_{3/4}O_2$ is synthesized as a high-performance low-cost cathode material for NIBs. Cooling rate after high temperature calcination is the key to synthesizing meso-structure controlled particles for NFMO material. It is found that quenching will produce hexagonal particles with no secondary structure while slowly cooling will produce sphere-like meso-structure controlled particles. The meso-structure of NFMO provides larger surface area, lower surface concentration of sodium carbonate, and higher Fe electrochemical activity, which together improve the electrochemical performance. Through this work we demonstrated that cooling rate is a vital parameter in synthesizing meso-structure controlled sodium ion cathode material and is an often overlooked avenue for controlling electrochemical performance. NFMO with sphere-like meso-structure and only with inexpensive elements represents a promising direction for the future development of cathode materials for NIBs.

ORCID

Hayley Hirsh ⓘ https://orcid.org/0000-0002-8105-6975

References

1. B. Dunn, H. Kamath, and J.-M. Tarascon, *Science (80-.)*, **334**, 928 (2011).
2. C. Delmas, *Adv. Energy Mater.*, **1703137**, 1703137 (2018).
3. Y. Jiang et al., *Adv. Energy Mater.*, **5**, 1 (2015).
4. J. Z. Guo et al., *Chem. - A Eur. J.*, **21**, 17371 (2015).
5. Y. You, X. L. Wu, Y. X. Yin, and Y. G. Guo, *Energy Environ. Sci.*, **7**, 1643 (2014).
6. J. Song et al., *J. Am. Chem. Soc.*, **137**, 2658 (2015).
7. F. Wan et al., *Nano Energy*, **13**, 450 (2015).
8. A. K. Padhi, K. S. Nanjundaswamy, and J. B. Goodenough, *J. Electrochem. Soc.*, **144**, 1 (1997).
9. N. Ortiz Vitoriano, N. Drewett, E. Gonzalo, and T. Rojo, *Energy Environ. Sci.*, (2017).
10. J. Alvarado et al., *ACS Appl. Mater. Interfaces*, acsami.7b05326 (2017).
11. X. Li et al., *Chem. Mater.*, **28**, 6575 (2016).
12. H. Wang et al., *J. Electrochem. Soc.*, **163**, A565 (2016).
13. M. Zhang, H. Liu, Z. Liu, C. Fang, and Y. S. Meng, *ACS Appl. Energy Mater.*, **1**, 3369 (2018).
14. Y. Zhuo et al., *J. Electrochem. Soc.*, **166**, A10 (2019).

15. K. S. Lee, S. T. Myung, H. J. Bang, S. Chung, and Y. K. Sun, *Electrochim. Acta*, **52**, 5201 (2007).
16. L. Mu et al., *J. Mater. Chem. A*, **00**, 1 (2018).
17. B. Tiwari and I. Bhattacharya, *Electrochim. Acta*, **270**, 363 (2018).
18. T.-Y. Yu, J.-Y. Hwang, D. Aurbach, and Y.-K. Sun, *ACS Appl. Mater. Interfaces*, **9**, 4534 (2017).
19. M. Islam, M. Jeong, J. Hwang, I. Oh, and Y. Sun, *Electrochim. Acta*, **258**, 220 (2017).
20. M.-H. Lee, Y.-J. Kang, S.-T. Myung, and Y.-K. Sun, *Electrochim. Acta*, **50**, 939 (2004).
21. S. H. Park, S. H. Kang, I. Belharouak, Y. K. Sun, and K. Amine, *J. Power Sources*, **177**, 177 (2008).
22. D. K. Lee et al., *J. Power Sources*, **162**, 1346 (2006).
23. X. He et al., *J. Power Sources*, **150**, 216 (2005).
24. M. A. Martin et al., *J. Electrochem. Soc.*, **162**, A991 (2015).
25. N. Yabuuchi et al., *Nat. Mater.*, **11**, 512 (2012).
26. J. Zhao et al., *J. Power Sources*, **264**, 235 (2014).
27. J. Chen et al., *Mater. Lett.*, **202**, 21 (2017).
28. V. Duffort, E. Talaie, R. Black, and L. F. Nazar, *Chem. Mater.*, **27**, 2515 (2015).
29. D. Nayak et al., *J. Solid State Electrochem.*, **4**, 133 (2017).
30. J. Park, G. Park, H. H. Kwak, S.-T. Hong, and J. Lee, *ACS Omega*, **3**, 361 (2018).
31. Y. Kee, N. Dimov, S. Champet, D. H. Gregory, and S. Okada, *Ionics (Kiel).*, **22**, 2245 (2016).
32. P. Vassilaras, A. J. Toumar, and G. Ceder, *Electrochem. commun.*, **38**, 79 (2014).
33. B. M. De Boisse, D. Carlier, M. Guignard, and C. Delmas, *J. Electrochem. Soc.*, **160**, 569 (2013).
34. M. H. Han et al., *Electrochim. Acta*, **182**, 1029 (2015).
35. S. Chu et al., *Ceram. Int.*, **44**, 5184 (2018).
36. H. Xu, J. Zong, and X. Liu, *Ionics (Kiel).*, 1939 (2018).
37. J. Hwang, S. Myung, D. Aurbach, and Y. Sun, *J. Power Sources*, **324**, 106 (2016).
38. D. Kim et al., *Electrochem. commun.*, **18**, 66 (2012).
39. C. Delmas, J.-J. Braconnier, C. Fouassier, and P. Hagenmuller, *Solid State Ionics*, **3–4**, 165 (1981).
40. G. K. Wertheim, S. Hüfner, and H. J. Guggenheim, *Phys. Rev. B*, **7**, 556 (1973).
41. M. Descostes, F. Mercier, N. Thromat, C. Beaucaire, and M. Gautier-Soyer, *Appl. Surf. Sci.*, **165**, 288 (2000).
42. A. P. Grosvenor, B. A. Kobe, M. C. Biesinger, and N. S. McIntyre, *Surf. Interface Anal.*, **36**, 1564 (2004).
43. I. Hasa, D. Buchholz, S. Passerini, B. Scrosati, and J. Hassoun, *Adv. Energy Mater.*, **4**, 1400083 (2014).
44. L. Zheng, L. Li, R. Shunmugasundaram, and M. N. Obrovac, *ACS Appl. Mater. Interfaces*, **10**, 38246 (2018).
45. D. W. Shin, C. A. Bridges, A. Huq, M. P. Paranthaman, and A. Manthiram, *Chem. Mater.*, **24**, 3720 (2012).
46. Y. Cao et al., *Adv. Mater.*, **23**, 3155 (2011).
47. B. D. McCloskey et al., *J. Phys. Chem. Lett.*, **3**, 997 (2012).
48. G. V. Zhuang et al., *J. Power Sources*, **134**, 293 (2004).
49. L. Zhang, W. Borong, L. Ning, and W. Feng, *Electrochim. Acta*, **118**, 67 (2014).